Magnetic and Contrast Properties of Labeled Platelets for Magnetomotive Optical Coherence Tomography

Amy L. Oldenburg,[†‡]* Caterina M. Gallippi,[‡] Frank Tsui,[†] Timothy C. Nichols,[§] Kellie N. Beicker,[†] Raghav K. Chhetri,[†] Dmitry Spivak,[†] Aaron Richardson,[‡] and Thomas H. Fischer[§]

[†]Department of Physics and Astronomy, [‡]Biomedical Research Imaging Center and Joint Department of Biomedical Engineering, and [§]Francis Owen Blood Research Laboratory and Department of Pathology and Laboratory Medicine, University of North Carolina, Chapel Hill, North Carolina

ABSTRACT   This article introduces a new functional imaging paradigm that uses optical coherence tomography (OCT) to detect rehydrated, lyophilized platelets (RL platelets) that are in the preclinical trial stage and contain superparamagnetic iron oxides (SPIOs) approved by the U.S. Food and Drug Administration. Platelets are highly functional blood cells that detect and adhere to sites of vascular endothelial damage by forming primary hemostatic plugs. By applying magnetic gradient forces, induced nanoscale displacements (magnetomotion) of the SPIO-RL platelets are detected as optical phase shifts in OCT. In this article, we characterize the iron content and magnetic properties of SPIO-RL platelets, construct a model to predict their magnetomotion in a tissue medium, and demonstrate OCT imaging in tissue phantoms and ex vivo pig arteries. Tissue phantoms containing SPIO-RL platelets exhibited >3 dB contrast/noise ratio at $\geq 1.5 \times 10^9$ platelets/cm^3. OCT imaging was performed on ex vivo porcine arteries after infusion of SPIO-RL platelets, and specific contrast was obtained on an artery that was surface-damaged ($P < 10^{-6}$). This may enable new technologies for in vivo monitoring of the adherence of SPIO-RL platelets to sites of bleeding and vascular damage, which is broadly applicable for assessing trauma and cardiovascular diseases.

INTRODUCTION

The ability to contrast a specific disease process in a whole organ or functional state of individual cells has become a major emphasis of biomedical imaging technology development (1). Cells are desirable targeting vehicles because they can easily be cultured or harvested in large quantities and naturally possess functional properties that man-made agents can only approximate. Dynamic information can be gained about the health or activity status of cells by means of noninvasive imaging of cells labeled with contrast agents. Recent advancements in cell-based imaging include labeling immune cells to detect and enhance inflammatory activity (2) and labeling stem cells to analyze tissue regeneration processes (3,4).

Platelets are particularly attractive as imaging vehicles, because they adhere to sites of endothelial disruption from a wide variety of pathological processes, are easily harvested from donor blood, and readily take up contrast agents through several mechanisms, including those involved with innate immunity. Their pathophysiological function is to detect and adhere to sites of vascular damage for the formation of primary hemostatic plugs, and then to amplify coagulation reactions to limit hemorrhage (5). Disruption of vascular endothelium and frank vascular breach can result from a wide variety of pathological processes, including mechanical damage in trauma as well as acute and chronic inflammation (6). The platelet is therefore a logical "plateform" for localizing imaging contrast agents and therapeutics to vascular sites where inflammatory processes perturb endothelial structure.

Rehydrated, lyophilized (RL) platelets (Stasix, Entegrion, Research Triangle Park, NC), employed in this study, are an infusion agent in preclinical trials for treating platelet-responsive bleeding. RL platelets are prepared from fresh human apheresis platelets by paraformaldehyde stabilization, and provide a solution to the logistical difficulties of platelet storage and harvesting (7). RL platelets have been shown to avidly adhere to wound sites (7) and display a broad-based functionality as a hemostatic agent in rabbit (8), canine (9), and porcine (10) bleeding models. RL platelets are an activatable hemostatic agent (11) that is removed from the free circulation within minutes by the reticuloendothelial system if not localized to sites of vascular injury (12). In this work, superparamagnetic iron oxides (SPIOs) comprised of MRI liver contrast agents (Feridex I.V., Advanced Magnetics, Lexington, MA) approved by the U.S. Food and Drug Administration are incorporated into platelets before paraformaldehyde stabilization. As we demonstrate here, the resulting SPIO-RL platelets maintain some hemostatic properties, while the SPIOs provide a magnetic handle by which to contrast the RL platelets.

Optical coherence tomography (OCT) is a biological imaging modality that provides noninvasive imaging on a scale similar to that of histology (i.e., at the cellular level), with millimeter-range imaging depth and micrometer-range resolution (13). It has been widely adapted clinically for ophthalmology (14), and increasingly applications are being developed for imaging of the coronary artery (15), skin (16), and upper airway (17), among other areas of interest (18).

Magnetomotive OCT (MMOCT) is an emerging technique for contrasting magnetic agents that exhibit a high magnetic susceptibility against a tissue background, by magnetically inducing nanoscale motions at a specific modulation frequency during acquisition of an OCT image (19,20). SPIOs are therefore excellent MMOCT contrast agents, because they exhibit magnetic susceptibilities that are $\sim 10^5$ times greater than that of human tissue, including red blood cells (21). The low modulation frequencies employed in MMOCT (1–1000 Hz) avoid heating due to magnetic fluid hyperthermia that typically occurs above 100 kHz (22). MMOCT has recently been applied to track SPIOs labeled with HER2neu antibodies targeting a breast cancer animal model in vivo (23).

In this article, we characterize the efficacy with which MMOCT can be used to contrast SPIO-RL platelets. Experiments are performed in tissue phantoms and porcine arteries using SPIO-RL platelets at concentrations expected to be similar to those in a typical in vivo infusion application for targeting sites of vascular damage. Characterization of the SPIO-RL platelet magnetic and contrast properties provide insight into the strengths and limitations of this technique. Because platelet-activating events are ubiquitous in many disease processes, the ability to study the highly dynamical function of platelets in flowing blood may provide fundamental knowledge about hemostasis arising from trauma and thrombosis, as well as vascular damage arising from cardiovascular disease and certain cancer therapies. Specific applications enabled by this technology may include intravascular OCT imaging for the assessment of thrombosis, and external OCT imaging for monitoring the efficacy of SPIO-RL platelets to detect bleeding during treatment for burn trauma.

MATERIALS AND METHODS

Preparation of SPIO-RL platelets

In this work, SPIOs consisted of an infusible magnetic resonance imaging liver contrast agent known as Feridex (a ferumoxides injectable solution; Advanced Magnetics), which is comprised of ~5-nm SPIO cores with a dextran coating (24) and a reported iron content of 11.2 mg Fe/mL. SPIOs were diluted 1/10 from infusion-grade stock, combined with apheresis platelets at $1 \times 10^9/\text{cm}^3$, and incubated overnight, which resulted in internalization of the SPIOs. After SPIO internalization, the nanoparticle-loaded platelets are separated from extracellular SPIO with size-exclusion chromatography and then stabilized with paraformaldehyde, by the same procedures used for the production of RL platelets (7), to obtain SPIO-RL platelets.

Imaging phantoms and samples for magnetic characterization were gelled in 1% w/v molecular-biology-grade agarose as an aqueous matrix with diamagnetic properties similar to that of tissue, and with a mass of nominally 0.2 g. For mass spectrometry and superconducting quantum interference device (SQUID) magnetometry, positive control samples were prepared with varying SPIO concentrations (200×, 400×, 600×, 1000×, and 2000× dilutions and control in citrated saline). Samples of SPIO-RL platelets and negative control RL platelets were prepared in citrated saline at 0.5×10^9 platelets/cm^3 as determined by hemocytometry. For details of MMOCT sample preparation, see Table S1 in the Supporting Material, where the dilutions of SPIO for positive-control samples were chosen to match the Fe concentrations of the various SPIO-RL samples. Mixtures of SPIO-RL and control RL platelets were employed to keep the net concentration of platelets constant, thus controlling for any effects due to platelets mechanically stiffening the matrix. Samples for MMOCT were also combined with 0.5 mg/mL TiO_2 micropowder (previously found to have insignificant magnetization (20)) to provide optical scattering.

Characterization of SPIO uptake by RL platelets

Inductively coupled plasma mass spectrometry (820-MS, Varian, Palo Alto, CA) was employed to independently quantify iron uptake into platelets. Samples of varying SPIO concentration were used for calibration. All samples were digested overnight in trace-metal-grade nitric acid (5.67 mL/g sample) and diluted 10× with deionized water. A calibration line ($R^2 > 0.99$) related the expected SPIO Fe content (using the manufacturer's value of 11.2 mg Fe/mL) to the mass spectrometer reading. This was then used to compute the Fe concentration in the platelet samples. Transmission electron microscopy of SPIO-RL platelets was performed as detailed elsewhere (25).

A colorimetric assay was used to quantify iron uptake into platelets as follows. SPIOs exhibit a broad visible absorption band from the ultraviolet up to 500 nm (brown), which contributes to the otherwise flat (white) scattering spectrum of RL platelets. The total attenuation (scattering plus absorption) measured at 370 nm (A_{370}) is therefore a sum of both RL platelets and SPIO content, whereas the ratio of attenuation values at 370 nm to those at 600 nm (A_{370}/A_{600}) is a function of the SPIO content in the platelet mixture (either added externally as a standard, or internalized in the platelets). Suspensions of RL platelets at $0.2 \times 10^9/\text{cm}^3$ were prepared, and varying amounts of SPIO were added in amounts corresponding to the range $0-150$ fg Fe/platelet. A standard curve of A_{370}/A_{600} versus Fe content/platelet was then used to quantify the Fe content of SPIO-RL platelets based upon their attenuation spectra.

Characterization of the magnetic properties of SPIO-RL platelets

To determine the efficacy of SPIO-RL platelets as magnetomotive contrast agents, we characterized their magnetic properties using SQUID magnetometry. (Note that Gaussian units or cgs emu are used in this article unless stated otherwise. The two are the same for magnetic properties). The magnetic properties of both SPIO-RL platelets and SPIO alone were measured to probe any differences due to SPIO internalization by the platelets. Diamagnetic plastic capsules (Quantum Design, San Diego, CA) were loaded with ~100 μL of each sample. A 5T SQUID magnetometer (MPMS, Quantum Design) was used to measure magnetization versus field hysteresis loops at 20°C. Temperature-dependent field-cooled (FC) and zero-field-cooled (ZFC) measurements at low fields between 50 and 2000 Oe were also performed for SPIO-RL platelets and 200× SPIO samples to probe the nature of their magnetic behavior. A typical ZFC measurement involved first cooling the sample in nominal zero field from 300 to 5 K, and then applying the field, with the measurement performed in the field as the temperature was warmed to 360 K. The FC counterpart was performed as the temperature was cooled from 360 K.

To accurately assess magnetic properties of dilute magnetic materials in a biological medium, care must be taken to account for the diamagnetic background of the medium (26). We addressed this by modeling the field-dependent magnetizations of the superparamagnetic SPIO using a Langevin function (first term in Eq. 1) and the weak diamagnetic or paramagnetic contributions from the other constituent parts of the sample (the second term in Eq. 1):

$$m(H) = M_s m_S \left(\coth\left(\frac{3\chi_S H}{M_s}\right) - \frac{M_s}{3\chi_S H} \right) + \left(\chi_m m_m + \chi_p n_p + \chi_h m_h \right) H. \tag{1}$$

In this expression, m is the total magnetization; H is the applied magnetic field; M_s is the saturation magnetization of the SPIO/mass of Fe; χ_s, χ_m, and χ_h are the magnetic susceptibilities/mass of Fe in the SPIOs, the medium (agarose and saline), and the plastic capsules, respectively; and m_s, m_m, and m_h are the masses corresponding to the χ values. The respective parameters for the platelets are χ_p, the magnetic susceptibility/number, and n_p, the total number. These terms are introduced to account for the possible contribution of paramagnetic iron in the platelets. For the SPIO-RL platelets, m_s is replaced by n_p, and thus, M_s and χ_s become the saturation magnetization and magnetic susceptibility/number of SPIO-RL platelets, respectively. For each sample, m_m and m_h were weighed, m_s was determined by the dilution factor of the SPIOs, and n_p was determined from the original dilution by hemocytometry. Control samples were measured to independently quantify χ_m, χ_p, and χ_h. Finally, χ_s and M_s were obtained for SPIO-RL platelets and SPIOs by least-squares fitting of the magnetization loops using Eq. 1.

Model of magnetomotive properties of SPIO-RL platelets

The measured magnetic properties were then used to create a computational model of the magnetic gradient force induced in a blood clot loaded with SPIO-RL platelets. We rewrite the magnetic gradient force equation in the absence of external current as

$$\frac{F}{V} = (M \cdot \nabla)B >> M_z(B_z, N_p)\nabla B_z$$
$$= M_z(B_z, N_p) f_{\text{magnet}} B_z, \qquad (2)$$

where force, F, per sample volume, V, is determined by the volume magnetization, M, and the gradient of the magnetic field, B. In our system, the gradient terms are dominated by the axial (z) components M_z and B_z. M_z is a function of B_z and platelet number density N_p. In the absence of eddy currents, an electromagnet can be described by a constant of proportionality, $f_{\text{magnet}} = \nabla B_z / B_z$, at a defined position relative to the magnet. This is useful in that increasing the magnet supply current results in a proportional increase in both B_z and ∇B_z. To model our system, we take $f_{\text{magnet}} = 100/\text{m}$ in the OCT imaging volume, because B_z changes by ~20% over the 2-mm imaging depth. We then rewrite Eq. 1 as

$$M_z(B_z, N_p) = \frac{m(B_z/\mu_0)}{V}$$
$$= M_s N_p \left(\coth(x B_z) - \frac{1}{x B_z} \right) + \chi_m B_z, \qquad (3)$$

where χ_m is now the volume magnetic susceptibility of the medium, taken to be -8.6×10^{-7} emu/cm^3 as an average value for human blood (21), $x = 3\chi_s/\mu_0 M_s$, χ_s and M_s are the per-platelet values (see Table 2), and μ_0 is the permeability of free space. The net magnetizations are sufficiently small to assume that $B_z = \mu_0 H_z$.

Porcine artery infusion experiments

To investigate their hemostatic properties, SPIO-RL platelets were perfused with ex vivo porcine arteries with and without luminal wall damage. Pigs from the Francis Owen Blood Research Laboratory were handled according to protocols approved by the Institutional Animal Care and Use Committee at the University of North Carolina at Chapel Hill. A mesenteric artery was obtained from a 6-year-old normocholesterolemic pig (serum cholesterol level 61 mg/dl) that had no gross evidence of atherosclerosis at necropsy. It is important to note that normocholesterolemic pigs do not normally develop atherosclerosis, which only develops if the animal is fed a high-fat diet to induce hypercholesterolemia (27). As such, control

arteries obtained from the pig are undamaged and expected to elicit no platelet response.

SPIO-RL platelet-containing blood was prepared by mixing one part SPIO-RL platelets at $2 \times 10^9/\text{cm}^3$ in citrated saline with nine parts porcine blood collected in citrate anticoagulant. The resulting SPIO-RL platelet concentration was $0.2 \times 10^9/\text{cm}^3$, and the endogenous platelet concentration was $0.243 \times 10^9/\text{cm}^3$. Immediately before infusion, the SPIO-RL platelet-blood mixture was recalcified by adding 1M CaCl$_2$ to achieve a 10-mM calcium ion concentration. Two segments of the mesenteric artery, each ~3 cm long, were flushed with citrated saline to remove endogenous blood and dissected from surrounding connective tissues. One segment was injured or deendothelialized using a 1-mm cytology brush (Wilson-Cook Medical, Winston Salem, NC) by making five passes through the vessel lumen. The other segment, used as a control, remained uninjured. One end of each of the segments (damaged and control) was ligated with a 5 Fr catheter, and 1.0 mL of the SPIO-RL platelet-blood mixture was infused at a steady rate for 4 min. The vessels were subsequently flushed with saline and cut into three segments, each ~1 cm long, for imaging. A portion of a blood clot was removed from one section of the damaged artery for imaging. As a control clot, citrated blood was drawn from another normocholesterolemic pig and coagulated by recalcification as described above.

At the volume flow rate in this experiment (4.2 mm^3/s through vessels 3–5 mm in diameter) the maximum value for the shear rate is estimated using the Poisseuille equation (28) to be 1.6/s, smaller than those typical of arterial or venous blood (29). This shear rate may overestimate the actual values, because the Poisseuille equation assumes a rigid cylindrical wall and Newtonian blood, which typically results in over-estimation of the actual shear rate (28). Therefore, we expect that the experimental shear rate value is well below that required for shear-induced platelet activation (30).

Magnetomotive OCT

A phase-resolved, spectral-domain OCT system was constructed to track the induced magnetomotion of the SPIO-RL platelets (Fig. 1). The light source consisted of a Ti:Sapphire laser (Griffin, Kapteyn-Murnane Labs, Boulder, CO) producing ~125 nm of bandwidth centered near 810 nm, corresponding to a coherence length of ~2 μm in tissue phantoms. The source light was passed through a Faraday isolator and coupled into a single-mode fiber for guidance into the OCT interferometer. A free-space Michelson interferometer is comprised of a stationary reference arm consisting of a variable attenuator and retroreflector, and a sample arm consisting of x- and y-scanning galvanometer mirrors and a lens of 40 mm focal length to provide 16 μm of transverse resolution with a confocal parameter of ~0.5 mm. Nominally 10–14 mW of light power was delivered to the sample, and backscattered light was collected and interfered with the reference light at the beamsplitter. The output light was then delivered by a single-mode fiber to a spectrometer in which it was spectrally dispersed by a 600-lines/mm grating in Littrow, and imaged by a biconvex lens of 200 mm focal length onto 2048 pixels of a line-scan camera operated at 1 kHz (Piranha 2, Dalsa, Waterloo, Ontario, Canada). The signal/noise ratio of this system was determined to be >95 dB. The differential phase sensitivity was determined to be 170 mrad by acquiring M-mode data from a coverslip, which is equivalent to a displacement sensitivity of 11 nm.

A water-jacketed solenoid coil was constructed to deliver predominantly axially- (z-) directed magnetic field gradients into the $2 \times 2 \times 1.5$-mm ($x \times y \times z$) OCT imaging volume for tissue-phantom imaging. For porcine arteries, the OCT imaging volume in y was extended to 4 mm. The solenoid is powered by a computer-controlled 250-W power supply, allowing for the magnetic field and gradient to be modulated up to 0.15 T and 15 T/m, respectively. The magnetic field was modulated with a square-root sinusoid at 100 Hz to provide a purely sinusoidal gradient force. For phantom imaging, data was collected into $2500 \times 9 \times 1024$ pixels ($x \times y \times z$) by acquiring nine sequential B-mode ($x \times z$) images. For porcine artery imaging, data was collected the same way, except that 4000 pixels were
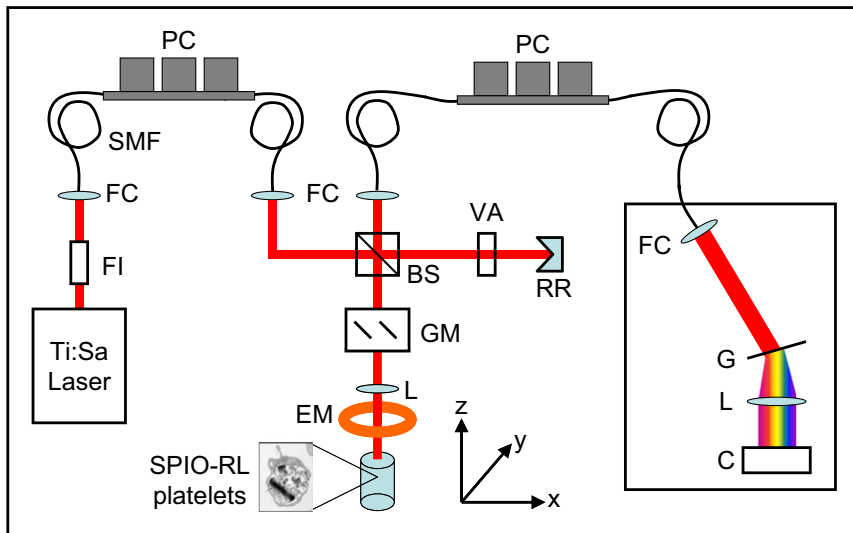
FIGURE 1 MMOCT system diagram (steering mirrors not shown). FI, Faraday isolator; FC, fiber coupler; SMF, single-mode fiber; PC, polarization controller; BS, beamsplitter; GM, galvanometer scanning mirrors; VA, variable attenuator; RR, retroreflector; L, lens; EM, electromagnet; G, grating; and C, camera.

obtained in x. Each B-mode image was processed according to a method described previously (20) in which a bandpass filter is employed at 100 Hz and an additional phase filter is employed to reject diamagnetic motion based upon the mechanical phase lag of the sample with respect to the driving magnetic waveform. Image-averaged values of the MMOCT signal were computed for each B-mode image and used to determine a mean and standard deviation signal value for each sample.

RESULTS

SPIO uptake by RL platelets

As shown in Fig. 2, SPIOs internalized by platelets occupy a significant fraction of the platelet volume, organizing into rodlike structures in the surface-connected open canalicular system (31). Each structure can contain hundreds of individual SPIOs (average core diameter ~5 nm). Table 1 summarizes the iron loading measured for SPIO-RL platelets compared to RL platelets alone. Values obtained by three different experimental techniques are in agreement

within experimental error. If we assume that the average platelet volume is 10.6 fL (32), the fractional volume occupied by the iron oxide cores of SPIOs in the RL platelets is estimated to be 0.15%. The dextran and citrate coatings, reported to be 5.6−9.1 and 0.25−0.53 mg/mL, respectively, in the SPIO solution would be expected to occupy an additional fractional platelet volume of 0.35−0.58% assuming a specific gravity of 1.

Magnetic properties of SPIO-RL platelets

The magnetic properties of SPIO-RL platelets, RL-platelet negative control, and SPIO positive control as measured by SQUID magnetometry are summarized in Table 2. We note that the χ_s and M_s of SPIO positive control is in agreement with previous measurements of ferumoxides (33). In addition, the magnetic susceptibilities of the gel medium and plastic holder are determined to be $(−6.3 \pm 0.4)$ and $(−6.1 \pm 0.7) \times 10^{-7}$ emu/g, respectively. The room-temperature field-dependent magnetization loops exhibit no remanence and no hysteresis within experimental uncertainty, as shown in Fig. S1 for a typical measurement with a best fit using Eq. 1. Temperature-dependent measurements (see Fig. S2) show FC and ZFC irreversibility (34). The ZFC behavior exhibits a characteristic peak at 50 K, and the onset of FC-ZFC irreversibility is ~100 K. The blocking temperature is expected to be between the two
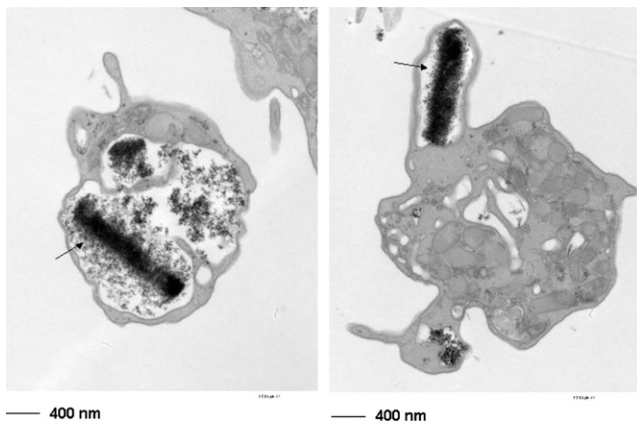

FIGURE 2 Transmission electron micrographs of SPIO-RL platelets. SPIOs display negative contrast in these transmission electron micrographs and are shown to organize into rodlike structures (*arrows*).

TABLE 1 Iron content of platelets determined by three experimental methods

Iron content of platelets (fg Fe/platelet)

	Colorimetric assay	Mass spectrometry	SQUID magnetometry*
RL platelets	—	3.0 ± 0.4	<5
SPIO-RL platelets	43 ± 11	48.3 ± 0.6	45 ± 7

*Magnetic forms of Fe only.

TABLE 2 Magnetic properties determined by SQUID magnetometry

Magnetic properties of platelets

	χ_s, magnetic susceptibility per mass (emu/g Fe)	χ_s, magnetic susceptibility per platelet (emu/platelet)	M_s, saturation magnetization/mass (emu/g Fe)	M_s, saturation magnetization per platelet (emu/platelet)
RL platelets control	-	$<9\times10^{-17}$	-	$(1 \pm 1)\times10^{-13}$
SPIO-RL platelets	$(6.5 \pm 1.0)\times10^{-2}$	$(3.2 \pm 0.5)\times10^{-15}$	84 ± 6	$(4.0 \pm 0.6)\times10^{-12}$
SPIO positive control	$(6.4 \pm 0.5)\times10^{-2}$	-	88 ± 7	-

temperatures, which is consistent with the literature value of ~60 K for ferumoxides (33).

The magnetic parameters χ_s and M_s for the SPIO-RL platelets obtained by analyzing the SQUID data are per platelet. The corresponding per-mass values were then calculated using the iron loading of 48.3 fg Fe/platelet measured by mass spectrometry, thus allowing for comparison between the SPIOs and SPIO-RL platelets. As shown in Table 2, the per-mass Fe values for magnetic susceptibility and saturation magnetization are the same for SPIOs and SPIO-RL platelets within experimental error.

Magnetomotive properties of SPIO-RL platelets

The measured magnetic properties were then used to create a computational model of the magnetic gradient force induced in a blood clot loaded with SPIO-RL platelets

according to Eqs. 2 and 3. As seen in Fig. S1, the diamagnetic contribution of an aqueous medium is nonnegligible when considering these forces. We find that the magnetic gradient force on SPIO-RL platelets over the range of concentrations used in our experiments is in the hundreds of μN/cm^3 (Fig. 3). Positive values correspond to net paramagnetic forces from the SPIOs, and negative values correspond to net diamagnetic forces from the tissue medium. It is important to point out that to maximize MMOCT imaging contrast, the maximum paramagnetic force at any given concentration is obtained at a magnetic field significantly less than 1 T. For smaller concentrations, the optimum magnetic field also becomes smaller, and it becomes increasingly important not to employ a large field to avoid a net negative force from the diamagnetic medium. The minimum SPIO-RL platelet concentration below which no net positive force is obtained is computed to be 0.27×10^9/cm^3.
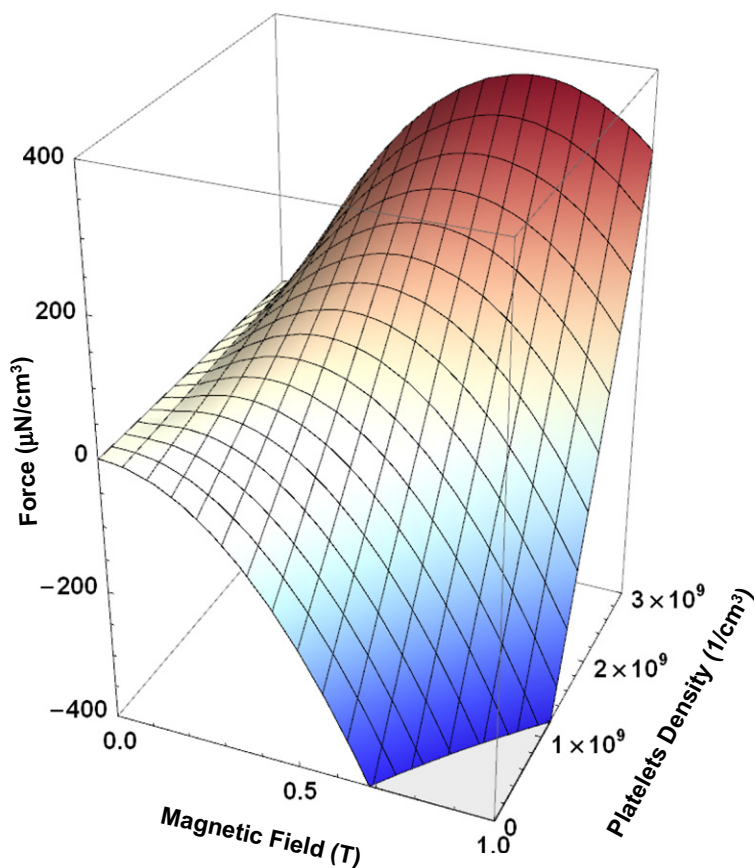

FIGURE 3 Magnetic-gradient force/volume as a function of platelet density and magnetic field in a blood medium, according to the computational model described in the text.

Magnetomotive OCT of SPIO-RL platelets in tissue phantoms

We found that SPIO-RL platelets exhibited high contrast via MMOCT in agarose scaffolds, in comparison to RL platelets (Fig. S3). In standard OCT imaging, the highly scattering TiO_2 micropowder is contrasted, and no difference between the RL platelets and SPIO-RL platelets can be observed ($P > 0.9$, n = 5, t-test, region of interest 0.1 mm^2). In MMOCT, specific contrast to the SPIO-RL platelets becomes evident. As noted in previous work (20), autocorrelation artifacts, which appear as vertical stripes immediately above the surface of the sample in the OCT images, are not observed in the MMOCT images. This is because magnetomotion is detected as relative motion between the sample and reference arms of the interferometer, whereas the autocorrelation signal is unchanged.

The concentration-dependent MMOCT signal was found for SPIOs and SPIO-RL platelets (Fig. 4), where the signal, as defined previously (20), is related to the amplitude of the sinusoidal sample displacement at the driving magnetic modulation frequency. This displacement amplitude is a function of both the SPIO concentration and the tissue elasticity. For concentrations at or above 1.5×10^9 platelets/cm^3, the MMOCT signal is significantly above the
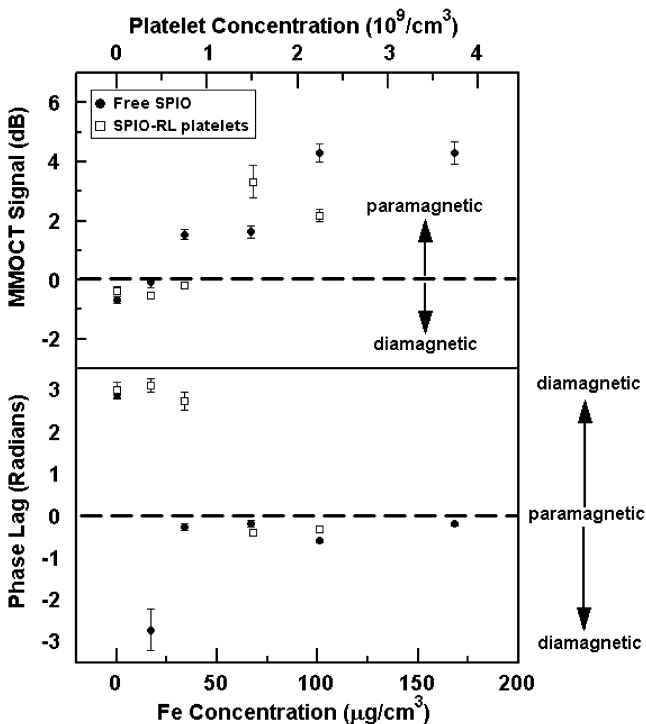

FIGURE 4 Image-averaged MMOCT signal (*upper*) and mechanical phase lag (*lower*) are plotted versus iron concentration for free SPIO positive control samples and SPIO-RL platelets. The corresponding platelet concentration is displayed on the top axis. Net paramagnetic and diamagnetic forces exhibit in-phase and out-of-phase motion, respectively, with the magnetic driving waveform.

background ($P < 0.0001$, n = 9, t-test). For both SPIOs and SPIO-RL platelets, a clear transition from net diamagnetic motion to net paramagnetc motion over increasing concentration is observed. Although the filter partially suppresses the diamagnetic signal, a small negative bias remains at zero concentration (nominally -0.5 ± 0.2 dB). Because diamagnetic motion is out of phase with the magnetic driving waveform, the phase lag at zero concentration is near $\pm \pi$. As the concentration is increased, the net force balance shifts to paramagnetic (in-phase) motion arising from the SPIOs. Thus, as the MMOCT signal increases, the phase lag simultaneously nears zero. Because there is a high magnetic field gradient in our system, a significant source of error arises from differences in the magnetic field at the sample due to its positioning (~30% change in force over 1 mm in depth), which is partially mitigated by aligning the sample surface to the same position within the OCT image. This may account for the apparent difference in the concentration threshold above which MMOCT contrast is obtained for the SPIOs and the SPIO-RL platelets. Also, saturation of the MMOCT signal occurs above ~3 dB. This occurs because the velocity of the magnetomotion becomes too large and causes a phase shift of $>\pi$ of the optical phase measured in successive samples by OCT, resulting in an underestimate of the magnetomotion when performing phase unwrapping. This is easily mitigated in practice by reducing the magnetic field strength to an appropriate value, or by increasing the camera sampling rate.

Imaging and hemostasis of SPIO-RL platelets in porcine arteries

To investigate the ability of SPIO-RL platelets to adhere to sites of vascular damage, they were perfused with ex vivo porcine arteries both with and without luminal wall damage. It was observed that a nonocclusive hemostatic plug (blood clot) had formed in the damaged artery after the 4-min infusion period, whereas the control exhibited no clotting.

Subsequently, MMOCT of damaged and control arteries was performed (Fig. 5 and Fig. S4). Arteries were imaged both uncut from the exterior, and cut longitudinally with the luminal wall exposed. Both cut and uncut control arteries exhibited MMOCT signals similar to control phantoms (Table 3). In the damaged artery, one cut segment exhibited signal similar to that of control, whereas a second segment exhibited MMOCT signals significantly larger than control signals both uncut and cut. It was noted that the first segment had displayed little macroscopic evidence of clotting (red color from trapped erythrocytes) compared to the second segment, which exhibited redness and large MMOCT signals. A portion of the clot from the damaged artery was also removed and found to have a large MMOCT signal and near-zero phase lag similar to diamagnetic samples, which was in contrast to the control clot. These
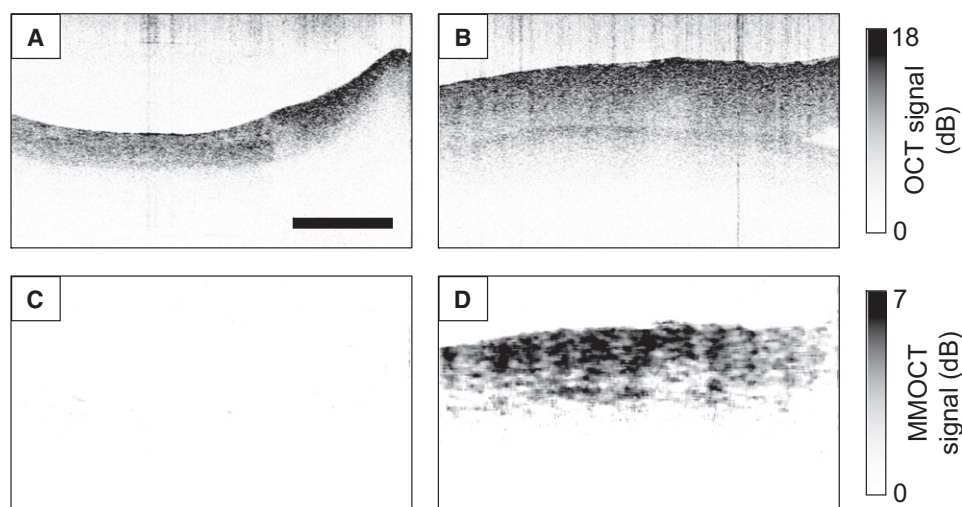
FIGURE 5 Sample B-mode images of ex vivo porcine arteries after exposure to SPIO-RL platelets in a flow chamber. (A) OCT of control artery. (B) OCT of damaged artery. (C) MMOCT of control artery. (D) MMOCT of damaged artery. These are longitudinally cut arteries with the luminal wall facing upward. Scale bar: 0.5 mm.

ex vivo studies, which mimic the vascular injuries that might be expected in some types of traumatic injury or vascular disorders, demonstrate that SPIO-RL platelets retain the native platelet functions that mediate localization to sites of endothelial damage.

DISCUSSION

SPIO uptake by RL platelets

The observation that platelets take up SPIO is not surprising in light of previous reports, where platelets have been noted to take up carbon (35), latex (36), cationic ferritin (37), colloidal gold (31), model viruses (38) and bacteria (39). Bacteria are occluded in the surface-connected open canalicular system (31,40), a system of membranes formed from invaginations of and spatially contiguous with the surface membrane. These observations suggest that platelets play a more important innate immune (host defense) role than is widely appreciated, and that SPIOs are accumulated through this set of immunity mechanisms.

Excellent agreement between three different experimental techniques (colorimetric, mass spectrometry, and SQUID magnetometry) lends a high degree of confidence to our measurement of the iron content of SPIO-RL platelets (43−48 fg/platelet). We found that although there is a signif-

icant fractional volume of iron oxide in the RL platelets (0.15%), the volume occupied by the SPIO coating molecules (dextran and citrate) is approximately three times larger. This suggests that reducing the coating material while maintaining the integrity of the colloidal dispersion may significantly increase the SPIO loading into RL platelets. It has also been suggested that dextran is undesirable as a stabilizing ligand, as it becomes easily dissociated in solution unless cross-linked (41).

Magnetic properties of SPIO-RL platelets

The dispersed SPIO and SPIO in RL platelets exhibit superparamagnetism. The behaviors of the two are nearly identical, including the superparamagnetic moment and the temperature dependence, despite the fact that the SPIOs inside RL platelets appear to be tightly packed (Fig. 2). This result indicates that the magnetic coupling between SPIO nanoparticles is weak. This is consistent with the results of previous work, where SPIOs of similar core size were shown to interact only weakly for interparticle spacings of $\sim >7$ nm (42), which is small compared to the expected spacing due to the coating molecules on our SPIO (~15 nm). However, these results do not rule out the role played by magnetic interactions in the formation of the rodlike structures in the RL platelets. Further study is needed to elucidate this. It is interesting to note that to

TABLE 3 Summary of MMOCT signals from ex vivo experiments in porcine arteries

Magnetomotive OCT of porcine arteries and clots

		MMOCT signal (dB)	MMOCT phase lag (rad)	P-value	Number of images
Control artery segment 1	Uncut	−0.44 ± 0.10	3.13 ± 0.21		9
Control artery segment 2	Cut	0.12 ± 0.15	−1.84 ± 1.04		9
Damaged artery segment 1	Cut	−0.30 ± 0.14	−2.90 ± 0.38	-	18
Damaged artery segment 2	Uncut	3.25 ± 0.93	−0.62 ± 0.06	$<10^{-6}$	9
Damaged artery segment 2	Cut	3.69 ± 0.55	−0.41 ± 0.05	$<10^{-6}$	7
Clot from normal blood		0.58 ± 0.69	−2.40 ± 1.30		9
Clot from damaged artery		2.07 ± 0.61	−0.72 ± 0.70	0.00018	9

our knowledge, there have been no previous reports of rod-shaped accumulation of magnetic or nonmagnetic particles in platelets. We note that during incubation of RL platelets with SPIOs, no external magnetic fields were present except that of the earth.

A magnetic-gradient-force model was employed to predict the response of a thrombus labeled with SPIO-RL platelets using the measured magnetic properties. According to the model, the magnetic-gradient forces range from tens to hundreds of $\mu N/cm^3$, depending on the platelet concentration and applied field. We chose a range of platelet concentrations up to $3 \times 10^9/cm^3$, which corresponds to ~0.9% volume loading of platelets. In comparison, a typical thrombus has been found to contain between 35−70% area (or, by extrapolation, 20−60% volume) of platelets (43). We expect that only a fraction of the platelets in a thrombus will be composed of SPIO-RL platelets during a typical infusion application, and therefore, $3 \times 10^9/cm^3$ is a reasonable estimate for the upper limit of platelet concentrations. It is important to note that this model allows us to predict the optimal applied magnetic field by which to maximize the net paramagnetic force. This optimum field is significantly less than 1T for the relevant range of platelet concentrations, because the nonnegligible tissue magnetization continues to grow larger for increasing fields after the SPIOs have reached saturation (~0.2 T). This relaxes the requirements on the electromagnet for the MMOCT system, permitting the use of a relatively small, water-jacketed solenoid coil.

Magnetomotive OCT of SPIO-RL platelets

In tissue phantoms, we observed significant MMOCT contrast of SPIO-RL platelets in 1% w/v agarose at concentrations $\geq 1.5 \times 10^9/cm^3$. Comparing this with predictions from our force model by assuming that the 1% agarose has an elastic modulus of 50 kPa (44) and a thickness of ~5 mm, we estimate, using Hooke's law, that a tissue displacement of 23 nm is obtained at this concentration. This is consistent with our OCT-system differential phase sensitivity of 11 nm, and it may explain why lower concentrations, although theoretically providing paramagnetic motion, were not contrasted due to displacements below our sensitivity. As a point of comparison, arteries are known to have an elastic modulus of 50−115 kPa (45), and abdominal aortic thrombi measured under tension have elastic moduli ranging from 42 to 540 kPa (46). In future work, it may be possible to significantly improve the phase sensitivity of the MMOCT system by the use of a common-path interferometer; such OCT systems have demonstrated sensitivities of <1 nm (47).

In ex vivo porcine arteries, we found that MMOCT signals of damaged artery were significantly larger than control when arteries were infused with SPIO-RL platelets. Because control clots untreated with SPIO-RL platelets

showed no significant MMOCT signal, we conclude that the activity of the SPIO-RL platelets caused the specific MMOCT contrast to the damaged arteries. These studies demonstrate that, as is the case with the native platelets, SPIO-RL platelets have the ability to adhere to sites of vascular injury and incorporate into blood clots. Futhermore, SPIO-RL platelets did not adhere in a measurable amount to uninjured endothelium, which suggests that they are not rendered prothrombotic and confirms the activatable nature of SPIO-RL platelet adhesion. In a previous study, the hemostatic function of RL platelets was shown to be mediated by primary hemostatic mechanisms working in concert with the activatable ability of the cell membrane to catalyze coagulation cascade turnover (11), and future studies are needed to compare these properties with that of the SPIO-RL platelets. It is important to point out that the activatable SPIO-RL platelet adhesion was demonstrated in the presence of endogenous platelets, as would be the case in most potential indications for this imaging therapeutic. As such, these ex vivo results are highly promising for the feasibility of employing SPIO-RL platelets to contrast sites of vascular damage in vivo.

CONCLUSIONS

By developing a force model, we predict that contrast of SPIO-RL platelets will be possible using MMOCT with a threshold concentration of 0.27×10^9 platelets/cm^3, where the diamagnetic and paramagnetic forces are exactly balanced. We found that around five times this concentration was needed in practice to detect SPIO-RL platelets using MMOCT, which corresponds to one SPIO-RL platelet out of ~80 native platelets in a typical thrombus. We also found that ex vivo porcine arteries exhibited specific MMOCT contrast when damaged and then exposed to SPIO-RL platelets. Although these results are encouraging with respect to potential applications in biomedical imaging of infusible SPIO-RL platelets, further study in vivo is needed to measure the efficiency with which SPIO-RL platelets label thrombi or other sites of arterial damage during a typical infusion application. Future improvement of the iron uptake efficiency of the platelets, perhaps by reducing the amount of the coating molecules currently occupying a large volume of the total SPIO footprint, may considerably improve the contrast of SPIO-RL platelets. We have demonstrated ex vivo that the SPIO-RL platelets specifically label sites of vascular damage, which may enable new technologies. This may include the use of intravascular OCT imaging for the detection of thrombosis, and exterior OCT imaging for monitoring the efficacy of SPIO-RL platelets during treatment for trauma.

SUPPORTING MATERIAL

REFERENCES

1. Wickline, S. A., and G. M. Lanza. 2003. Nanotechnology for molecular imaging and targeted therapy. *Circulation.* 107:1092–1095.

2. de Vries, I. J., W. J. Lesterhuis, …, C. G. Figdor. 2005. Magnetic resonance tracking of dendritic cells in melanoma patients for monitoring of cellular therapy. *Nat. Biotechnol.* 23:1407–1413.

3. Amsalem, Y., Y. Mardor, …, J. Leor. 2007. Iron-oxide labeling and outcome of transplanted mesenchymal stem cells in the infarcted myocardium. *Circulation.* 116(11, Suppl):I38–I45.

4. Corot, C., P. Robert, …, M. Port. 2006. Recent advances in iron oxide nanocrystal technology for medical imaging. *Adv. Drug Deliv. Rev.* 58:1471–1504.

5. Jurk, K., and B. E. Kehrel. 2005. Platelets: physiology and biochemistry. *Semin. Thromb. Hemost.* 31:381–392.

6. Polgar, J., J. Matuskova, and D. D. Wagner. 2005. The P-selectin, tissue factor, coagulation triad. *J. Thromb. Haemost.* 3:1590–1596.

7. Read, M. S., R. L. Reddick, …, K. M. Brinkhous. 1995. Preservation of hemostatic and structural properties of rehydrated lyophilized platelets: potential for long-term storage of dried platelets for transfusion. *Proc. Natl. Acad. Sci. USA.* 92:397–401.

8. Bode, A. P., and M. S. Read. 2000. Lyophilized platelets: continued development. *Transfus. Sci.* 22:99–105.

9. Bode, A. P., R. M. Lust, …, T. H. Fischer. 2008. Correction of the bleeding time with lyophilized platelet infusions in dogs on cardiopulmonary bypass. *Clin. Appl. Thromb. Hemost.* 14:38–54.

10. Hawksworth, J. S., E. A. Elster, …, D. K. Tadaki. 2009. Evaluation of lyophilized platelets as an infusible hemostatic agent in experimental non-compressible hemorrhage in swine. *J. Thromb. Haemost.* 7:1663–1671.

11. Fischer, T. H., A. P. Bode, …, M. S. Read. 2006. Primary and secondary hemostatic functionalities of rehydrated, lyophilized platelets. *Transfusion.* 46:1943–1950.

12. Fisher, T. H., E. Merricks, …, A. P. Bode. 2001. Splenic clearance mechanisms of rehydrated, lyophilized platelets. *Artif. Cells, Blood Substit., and Immobil. Biotech.* 29:439–451.

13. Huang, D., E. A. Swanson, …, G. Fujimoto. 1991. Optical coherence tomography. *Science.* 254:1178–1181.

14. Srinivasan, V. J., M. Wojtkowski, …, J. G. Fujimoto. 2006. High-definition and 3-dimensional imaging of macular pathologies with high-speed ultrahigh-resolution optical coherence tomography. *Ophthalmology.* 113:2054–2065, e1–e14.

15. Jang, I. K., G. J. Tearney, …, B. E. Bouma. 2005. *In vivo* characterization of coronary atherosclerotic plaque by use of optical coherence tomography. *Circulation.* 111:1551–1555.

16. Pierce, M. C., J. Strasswimmer, …, J. F. de Boer. 2004. Advances in optical coherence tomography imaging for dermatology. *J. Invest. Dermatol.* 123:458–463.

17. Armstrong, J. J., M. S. Leigh, …, P. R. Eastwood. 2006. Quantitative upper airway imaging with anatomic optical coherence tomography. *Am. J. Respir. Crit. Care Med.* 173:226–233.

18. Zysk, A. M., F. T. Nguyen, …, S. A. Boppart. 2007. Optical coherence tomography: a review of clinical development from bench to bedside. *J. Biomed. Opt.* 12:051403–051421.

19. Oldenburg, A. L., J. R. Gunther, and S. A. Boppart. 2005. Imaging magnetically labeled cells with magnetomotive optical coherence tomography. *Opt. Lett.* 30:747–749.

20. Oldenburg, A. L., V. Crecea, …, S. A. Boppart. 2008. Phase-resolved magnetomotive OCT for imaging nanomolar concentrations of magnetic nanoparticles in tissues. *Opt. Express.* 16:11525–11539.

21. Spees, W. M., D. A. Yablonskiy, …, J. J. Ackerman. 2001. Water proton MR properties of human blood at 1.5 Tesla: magnetic susceptibility, T(1), T(2), T*(2), and non-Lorentzian signal behavior. *Magn. Reson. Med.* 45:533–542.

22. Jordan, A., R. Scholz, …, R. Felix. 1999. Magnetic fluid hyperthermia (MFH): Cancer treatment with AC magnetic field induced excitation of biocompatible superparamagnetic nanoparticles. *J. Magn. Magn. Mater.* 201:413–419.

23. John, R., R. Rezaeipoor, …, S. A. Boppart. 2010. In vivo magnetomotive optical molecular imaging using targeted magnetic nanoprobes. *Proc. Natl. Acac. Sci.* 107:8085–8090.

24. Clément, O., N. Siauve, …, G. Frija. 1998. Liver imaging with ferumoxides (Feridex): fundamentals, controversies, and practical aspects. *Top. Magn. Reson. Imaging.* 9:167–182.

25. Sanders, W. E., M. S. Read, …, K. M. Brinkhous. 1988. Thrombotic thrombocytopenia with von Willebrand factor deficiency induced by botrocetin. An animal model. *Lab. Invest.* 59:443–452.

26. Hautot, D., Q. A. Pankhurst, and J. Dobson. 2005. Superconducting quantum interference device measurements of dilute magnetic materials in biological samples. *Rev. Sci. Instrum.* 76:045101–045104.

27. Brodala, N., E. P. Merricks, …, T. C. Nichols. 2005. Porphyromonas gingivalis bacteremia induces coronary and aortic atherosclerosis in normocholesterolemic and hypercholesterolemic pigs. *Arterioscler. Thromb. Vasc. Biol.* 25:1446–1451.

28. Papaioannou, T. G., and C. Stefanadis. 2005. Vascular wall shear stress: basic principles and methods. *Hellenic J. Cardiol.* 46:9–15.

29. Lipowsky, H. H., S. Usami, and S. Chien. 1980. In vivo measurements of "apparent viscosity" and microvessel hematocrit in the mesentery of the cat. *Microvasc. Res.* 19:297–319.

30. Kroll, M. H., J. D. Hellums, …, J. L. Moake. 1996. Platelets and shear stress. *Blood.* 88:1525–1541.

31. White, J. G. 2005. Platelets are covercytes, not phagocytes: uptake of bacteria involves channels of the open canalicular system. *Platelets.* 16:121–131.

32. Endler, G., A. Klimesch, …, R. Sunder-Plassmann. 2002. Mean platelet volume is an independent risk factor for myocardial infarction but not for coronary artery disease. *Br. J. Haematol.* 117:399–404.

33. Jung, C. W., and P. Jacobs. 1995. Physical and chemical properties of superparamagnetic iron oxide MR contrast agents: ferumoxides, ferumoxtran, ferumoxsil. *Magn. Reson. Imaging.* 13:661–674.

34. Joy, P. A., and S. K. Date. 2000. Comparison of the zero-field-cooled magnetization behavior of some ferromagnetic and ferrimagnetic systems. *J. Magn. Magn. Mater.* 218:229–237.

35. van Aken, W. G., T. M. Goote, and J. Vreeken. 1968. Platelet aggregation: an intermediary mechanism in carbon clearance. *Scand. J. Haematol.* 5:333–338.

36. White, J. G. 1972. Uptake of latex particles by blood platelets: phagocytosis or sequestration? *Am. J. Pathol.* 69:439–458.

37. Yamazaki, H., H. Suzuki, …, K. Tanoue. 1984. Electron microscopic observations on platelet aggregation induced by cationized ferritin. *Blood.* 63:439–447.

38. Bik, T., I. Sarov, and A. Livne. 1982. Interaction between vaccinia virus and human blood platelets. *Blood.* 59:482–487.

39. Clawson, C. C. 1973. Platelet interaction with bacteria. 3. Ultrastructure. *Am. J. Pathol.* 70:449–471.

40. White, J. G. 2006. Why human platelets fail to kill bacteria. *Platelets.* 17:191–200.

41. Peng, X.-H., X. Qian, …, D. M. Shin. 2008. Targeted magnetic iron oxide nanoparticles for tumor imaging and therapy. *Int. J. Nanomedicine.* 3:311–321.

42. Frankamp, B. L., A. K. Boal, …, V. M. Rotello. 2005. Direct control of the magnetic interaction between iron oxide nanoparticles through dendrimer-mediated self-assembly. *J. Am. Chem. Soc.* 127:9731–9735.

43. Sato, Y., K. Hatakeyama, …, Y. Asada. 2005. Proportion of fibrin and platelets differs in thrombi on ruptured and eroded coronary atherosclerotic plaques in humans. *Heart.* 91:526–530.

44. Benkherourou, M., C. Rochas, …, P. Y. Guméry. 1999. Standardization of a method for characterizing low-concentration biogels: elastic properties of low-concentration agarose gels. *J. Biomech. Eng.* 121:184–187.

45. Nichols, W. W., and M. F. O'Rourke. 1990. McDonald's Blood Flow in Arteries, 3rd ed. Edward Arnold, London.

46. Speelman, L., G. W. H. Schurink, …, M. H. Jacobs. 2010. The mechanical role of thrombus on the growth rate of an abdominal aortic aneurysm. *J. Vasc. Surg.* 51:19–26.

47. Choma, M. A., A. K. Ellerbee, …, J. A. Izatt. 2005. Spectral-domain phase microscopy. *Opt. Lett.* 30:1162–1164.